

Conformational Evolution of Elongated Polymer Solutions Tailors the Polarization of Light-Emission from Organic Nanofibers

Andrea Camposeo,^{*,†,‡} Israel Greenfeld,^{‡,‡,*} Francesco Tantussi,^{§,||} Maria Moffa,[†] Francesco Fuso,^{§,||} Maria Allegrini,^{§,||} Eyal Zussman,[‡] and Dario Pisignano^{*,†,⊥}

[†]National Nanotechnology Laboratory of Istituto Nanoscienze-CNR, via Arnesano, I-73100 Lecce, Italy

[‡]Department of Mechanical Engineering, Technion—Israel Institute of Technology, Haifa 32000, Israel

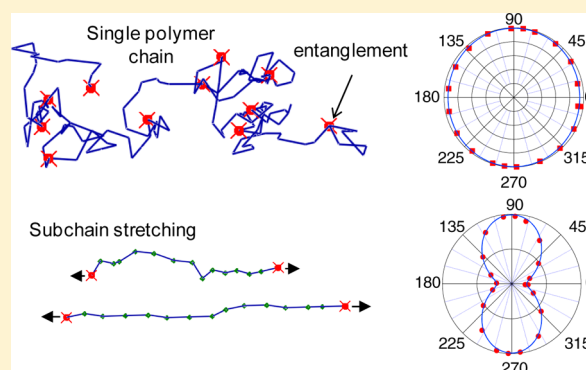
[§]Dipartimento di Fisica “Enrico Fermi” and CNISM, Università di Pisa, Largo Bruno Pontecorvo 3, I-56127 Pisa, Italy

^{||}Istituto Nazionale di Ottica INO—CNR, Sezione di Pisa, I-56127 Pisa (Italy)

[⊥]Dipartimento di Matematica e Fisica “Ennio De Giorgi”, Università del Salento, via Arnesano I-73100 Lecce, Italy

Supporting Information

ABSTRACT: Polymer fibers are currently exploited in tremendously important technologies. Their innovative properties are mainly determined by the behavior of the polymer macromolecules under the elongation induced by external mechanical or electrostatic forces, characterizing the fiber drawing process. Although enhanced physical properties were observed in polymer fibers produced under strong stretching conditions, studies of the process-induced nanoscale organization of the polymer molecules are not available, and most of fiber properties are still obtained on an empirical basis. Here we reveal the orientational properties of semiflexible polymers in electrospun nanofibers, which allow the polarization properties of active fibers to be finely controlled. Modeling and simulations of the conformational evolution of the polymer chains during electrostatic elongation of semidilute solutions demonstrate that the molecules stretch almost fully within less than 1 mm from jet start, increasing polymer axial orientation at the jet center. The nanoscale mapping of the local dichroism of individual fibers by polarized near-field optical microscopy unveils for the first time the presence of an internal spatial variation of the molecular order, namely the presence of a core with axially aligned molecules and a sheath with almost radially oriented molecules. These results allow important and specific fiber properties to be manipulated and tailored, as here demonstrated for the polarization of emitted light.



by stimulated emission,¹⁶ the macroscopic quantum spatial coherence of the exciton state,¹⁷ and the polarization of emitted light. In general, stretching a semidilute polymer solution by an electrostatic field is very effective to prime the formation of fibers, potentially resulting in a structure mostly composed of ordered and aligned chains.^{18–20} Little is known however about the nanoscale features induced by elongational dynamics and about how these features can be exploited to tailor and control macroscopic properties of solid nanostructures.

In this paper, we employ the unique features of scanning near-field optical microscopy (SNOM)^{21–23} to investigate at nanoscale polymer fibers produced by electrospinning. Absorption measurements with nm-spatial resolution and polarization modulation provide insight into the nanoscale variation of molecular alignment, evidencing an unexpected change from axial to radial molecular orientation upon moving

by stimulated emission,¹⁶ the macroscopic quantum spatial coherence of the exciton state,¹⁷ and the polarization of emitted light. In general, stretching a semidilute polymer solution by an electrostatic field is very effective to prime the formation of fibers, potentially resulting in a structure mostly composed of ordered and aligned chains.^{18–20} Little is known however about the nanoscale features induced by elongational dynamics and about how these features can be exploited to tailor and control macroscopic properties of solid nanostructures.

In this paper, we employ the unique features of scanning near-field optical microscopy (SNOM)^{21–23} to investigate at nanoscale polymer fibers produced by electrospinning. Absorption measurements with nm-spatial resolution and polarization modulation provide insight into the nanoscale variation of molecular alignment, evidencing an unexpected change from axial to radial molecular orientation upon moving

Received: February 21, 2014

Revised: June 23, 2014

INTRODUCTION

Fibers^{1–4} are typically formed upon the solidification of a tiny filament drawn from a viscous polymer solution or melt,^{5–7} whose thinning follows a very complex dynamics.^{8–10} Understanding how polymer chains modify their conformation at nanoscale, and to what extent they keep their configuration in solid nanostructures, is fundamental for many applications and for controlling the resulting physical properties of fibers.^{11,12} For example, polymers are typically considered bad thermal conductors, but aligning their chains in 1-dimensional (1D) nanostructures allows their thermal conductivity to be improved approaching the single-molecule limit (about 350 W m⁻¹ K⁻¹ for polyethylene).⁵ Similarly, charge mobilities (μ) in organic semiconductor films are typically low (most often <10⁻¹ V cm⁻² s⁻¹), although in single π -conjugated polymer chains μ can be of the order of hundreds of V cm⁻² s⁻¹.¹³ In the bulk, the disordered supramolecular assembly limits the charge mobility, whereas 1D nanostructures show an increase of 1–3 orders of magnitude of μ .^{14,15} The alignment of π -conjugated molecules is also effective to improve the amplification of light

from the fiber axis to its surface. The formation of such complex structures occurs close to the polymer jet start, as demonstrated by modeling the evolution of the conformation of the polymer chains network.

EXPERIMENTAL SECTION

Conjugated Polymer Nanofibers. Fibers are produced by electrospinning a solution (70–200 μM polymer) of poly[2-methoxy-5-(2-ethylhexyloxy)-1,4-phenylenevinylene] (MEH-PPV) (molecular weight 380 000 g/mol, American Dye Source Inc.). Sprayed films of microbeads and microfibers are obtained at concentrations $>200 \mu\text{M}$. The polymer is dissolved in a 1:4 (weight:weight) mixture of dimethyl sulfoxide (DMSO) and tetrahydrofuran (THF). The electrospinning system consists of a microprocessor dual drive syringe pump (33 Dual Syringe Pump, Harvard Apparatus Inc.), feeding the polymer solution through the metallic needle at constant rate (10 $\mu\text{L}/\text{min}$). A 11 kV bias is applied between the needle and a metallic collector (needle-collector distance 6 cm), made of two Al stripes positioned at a mutual distance of 2 cm. The MEH-PPV nanofibers are collected on a $1 \times 1 \text{ cm}^2$ quartz substrate for optical investigation. Arrays of uniaxially aligned nanofibers are also produced by using a rotating collector (4000 rpm, corresponding to a linear velocity of 30 m/s at the disk edge) for emission polarization measurements, featuring similar morphology and optical properties as samples deposited on the Al stripes. The fiber morphology is investigated by scanning electron microscopy (SEM) using a Nova NanoSEM 450 system (FEI), with an acceleration voltage of 5–10 kV.

Polarized Emission. Optical images of the fibers are obtained by confocal microscopy, using an inverted microscope (Eclipse Ti, Nikon) equipped with a confocal laser scanning head (AIR MP, Nikon). An Ar^+ ion laser ($\lambda_{\text{exc}} = 488 \text{ nm}$) excites the fibers through an oil immersion objective with numerical aperture, $\text{N.A.} = 1.4$. The intensity of the light transmitted through the sample, measured by a photomultiplier, is recorded synchronously to the confocal acquisition of the laser-excited fluorescence. The polarization of the emission of individual nanofibers at different polymer concentrations is characterized by a microphotoluminescence system, composed by a diode laser excitation source ($\lambda = 405 \text{ nm}$) coupled to an inverted microscope (IX71, Olympus). The laser beam propagates perpendicular to the substrate on which the fiber is deposited, and it is focused on the sample through a 20 \times objective ($\text{N.A.} = 0.5$, spot size 30 μm). Furthermore, the fiber is positioned with its longitudinal axis almost parallel to the incident laser polarization. The PL emitted by individual nanofibers is collected along the direction perpendicular to the substrate, by means of an optical fiber, and dispersed in a monochromator (USB 4000, Ocean Optics). The polarization of the emission is analyzed by a polarization filter mounted on a rotating stage and positioned between the emitting MEH-PPV nanofiber and the collecting optics. The system response is precisely analyzed in order to avoid artifacts due to the collection and measurement apparatus.

SNOM. A polarization-modulation near field microscopy system is used to analyze the linear dichroism of tens of individual MEH-PPV fibers. The SNOM system, operating in emission mode, excites samples in the optical near-field of a tapered optical fiber probe (Nanonics), with a nominal aperture of 50 nm, delivering a near-field power up to the tens of nW range ($\lambda = 473 \text{ nm}$). The signal transmitted by the samples is collected by an aspherical lens ($\text{N.A.} = 0.55$, diameter of 13 mm) and sent onto a photomultiplier. The polarization modulation relies on a photoelastic modulator (PEM-100, Hinds Instruments), behaving as a waveplate with periodically modulated retardation. The modulator is followed by a $\lambda/4$ waveplate and the whole system is conceived in order to send into the optical fiber probe radiation linearly polarized along a direction periodically oscillating in the transverse plane. The photomultiplier signal is split and sent into two different digital dual lock-in amplifiers (Stanford Research SR830DSP). The first one, referenced to the polarization modulator frequency, f , provides with an output (hereafter called AC)

representative of the sample response to polarized radiation, whereas the second lock-in, referenced to a slow modulation frequency f' ($f/f' > 10$) of the laser amplitude, is used to determine the optical transmission averaged over all polarization states (DC output).

The dichroic ratio of sample, $\gamma = ((I_{\parallel} - I_{\perp}) / (I_{\parallel} + I_{\perp}))$, where I_{\parallel} and I_{\perp} are the transmitted intensity for polarization aligned along two mutually orthogonal directions, respectively, is quantitatively evaluated from the ratio AC/DC. This requires to model the behavior of the whole optical chain and to account for the residual optical activity of its components, including the optical fiber probe (see Supporting Information). Indeed, reference measurements performed on bare substrates provide a dichroic ratio around zero as expected (see also Supporting Information). Moreover, the polarization state of the light incident on the sample is also characterized, by rotating the linear polarization of the light coupled into the SNOM fiber using a $\lambda/2$ waveplate, and measuring the intensity transmitted by a linear polarizer used as sample for each position of the $\lambda/2$ waveplate (see also Supporting Information). We have measured a ratio between the maximum and the minimum intensity transmitted by the polarizer in the range 10^1 – 10^2 . Overall, calibration experiments allow any contribution of the measurement setup to the obtained results to be ruled out.

RESULTS AND DISCUSSION

Figure 1 shows SEM pictures of MEH-PPV fibers produced by electrospinning solutions with different polymer concentra-

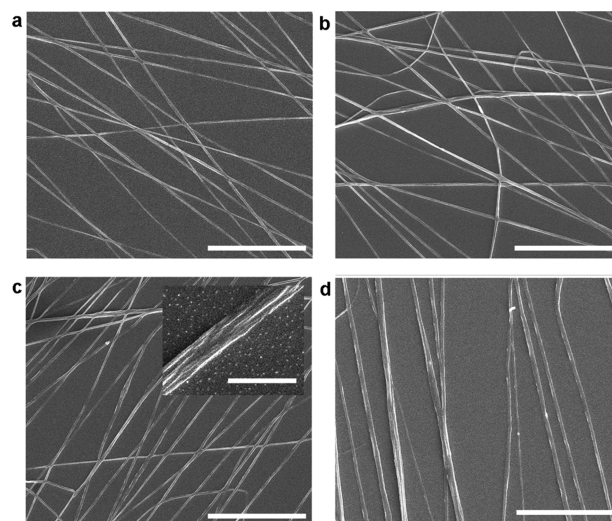


Figure 1. SEM images of electrospun MEH-PPV fibers realized by varying the solution polymer concentration in the range 70–200 μM . The corresponding polymer volume fraction, ϕ , is 0.025 (a), 0.036 (b), 0.054 (c), and 0.064 (d), respectively. Scale bar: 20 μm . Inset in part c: Zoomed micrograph of an individual fiber highlighting its ribbon shape. Scale bar: 2 μm .

tions. The fibers generally feature a ribbon shape, with average width in the range 500–600 nm and width:height ratio of about 10:1. The average fiber width increases by roughly 30% upon increasing the polymer concentration in the 70–200 μM range. In addition, fibers emit bright light, allowing the chain order to be investigated by optical methods (Figure 2a). Figure 2b shows the confocal transmission micrograph of excitation laser light, collected by crossed polarizers (analyzer axis perpendicular to the incident laser polarization), for nanofibers positioned at 0° , 65° , and 90° with respect to the incident laser polarization. A significant transmitted signal can be measured only for fibers positioned at 65° , indicating optical

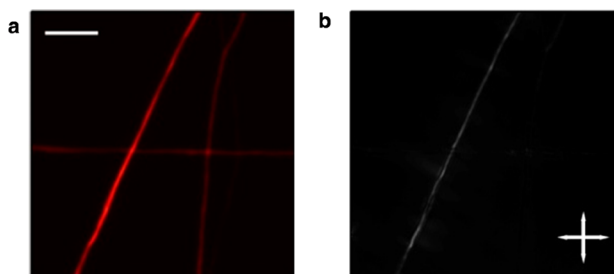


Figure 2. (a) Fluorescence confocal micrograph of conjugated polymer fibers. Scale bar: 10 μm . (b) Confocal map of the exciting laser intensity transmitted by the fibers, collected simultaneously to the emission map in part (a). The polarization of the excitation laser (highlighted by the horizontal arrow) is aligned parallel to the longitudinal axis of the horizontal fiber, whereas the axis of the analyzer (highlighted by the vertical arrow) is positioned perpendicularly to the incident laser polarization.

anisotropy which is expectedly the result of a preferential molecular alignment along the fiber length.

Polarized near-field absorption microscopy (Figure 3a) provides a direct measurement of the spatial variation of polymer alignment, through the map of the local dichroism, γ , i.e. the normalized difference between the transmission of radiation polarized along two mutually orthogonal directions. The map (Figure 3b) is determined by the distribution and anisotropy of absorbing chromophores (see Supporting Information). Here, the most important finding is the spatial variation of dichroism and, consequently, of molecular alignment (Figure 3c). Unexpectedly, the sign of the dichroic ratio, γ , is not constant throughout the fiber, because of regions showing preferential absorption of light polarized along or across the fiber axis (for the scan shown, they correspond to negative or positive γ , respectively).

These results suggest the presence of a core, with width $\sim 40\%$ of fiber diameter, where chromophore dipoles preferentially align along the fiber length, whereas molecules closer to the fiber border show a preferential radial orientation. The decrease of the dichroic ratio from positive to null values nearby the fiber edges (i.e., for positions roughly $\leq 0.5 \mu\text{m}$ and $\geq 1.5 \mu\text{m}$ according to the horizontal axis of Figure 3c) may be, instead, affected by the local curvature of the ribbon-shaped

fibers and will not be considered in the following analysis. To learn more about the origin of the found spatial variation of the molecular alignment, we use a model of the polymer network and perform simulations of its dynamics, as previously developed for fully flexible and semiflexible polymer chains.^{24–26} Simulations are here aimed at better rationalizing the observed chain orientation in the core, and at assessing the relevant process variables determining such orientation, thus ultimately allowing the macroscopic physical properties of the electrospun fibers to be tailored and controlled. In this approach, a semiflexible conjugated polymer chain is modeled as a series of N rigid segments, each of length $b = nd$ (n spherical beads of diameter $d \cong 1.2 \text{ nm}$, each bead consisting of two chemical monomers). The segment length b represents the average distance between two neighboring bonding defects along the chain backbone, where a bonding defect introduces local flexibility in the chain.²⁷ The corresponding defects concentration, using two chemical monomers per bead, is $(2n)^{-1}$ of monomers. The chain conformational correlation is lost above the scale of a segment due to the bonding defects, and therefore the rigid segment b is regarded as a Kuhn segment, and a freely jointed chain model is assumed. Fully flexible polymers are a particular case of the model ($n = 1$),²⁴ and generality is retained by using the segmental aspect ratio parameter, n , to specify the degree of chain flexibility.

In general, the high entanglement of chains creating a connective network determines the viscoelastic property of semidilute solutions. An entanglement can be simply defined as a topological constraint that inhibits intercrossing of two chains. The conformation of the entangled polymer network in the semidilute solution and the interactions relevant to the solvent type are described by scaling laws. When the segmental aspect ratio is high, an entanglement strand (i.e., a chain section between two adjacent entanglements) has the same length scale as the network correlation length (mesh size), ξ , the end-to-end distance of an unperturbed subchain containing N_s rigid segments. Given the aspect ratio n , polymer volume fraction ϕ , and solution properties expressed by Flory's exponent,²⁸ ν and Flory's interaction parameter, χ , the number of rigid segments in a subchain for good solvents is (Supporting Information):

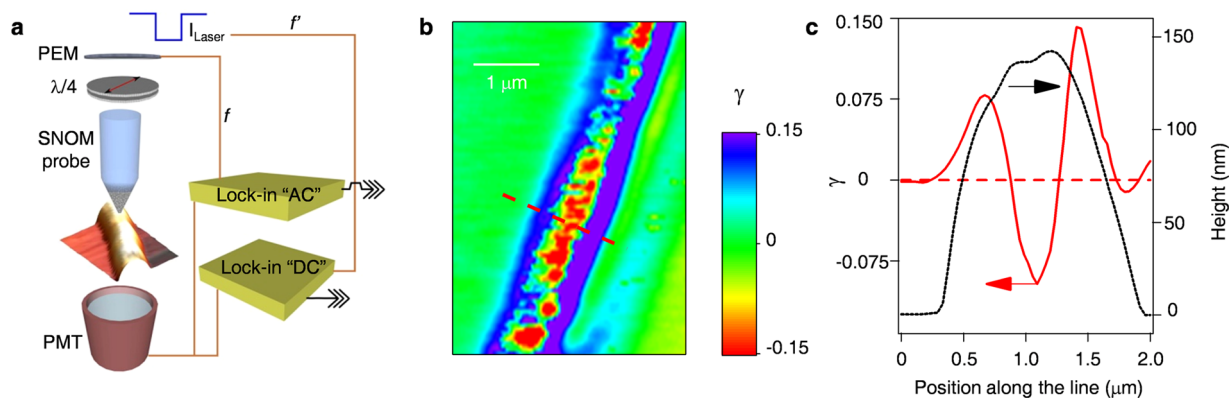


Figure 3. (a) Schematics of the polarization-modulation SNOM measurement. PEM: photoelastic modulator, PMT: photomultiplier. (b) Map of the dichroic ratio of a single MEH-PPV fiber. The dichroic ratio is zero for nonoptically active regions (background contribution subtracted, see Supporting Information). (c) Line profile analysis displaying the cross sections, along the dashed segment in part b, of γ (continuous line) and of topography got simultaneously with the optical data (dotted line). The change in sign of γ when crossing the fiber (dashed horizontal line corresponding to $\gamma = 0$) indicates different alignments of the polymer with respect to the fiber axis.

$$N_s \approx \left(\frac{n}{1-2\chi} \right)^{3(2\nu-1)/(3\nu-1)} (n^2\phi)^{-1/(3\nu-1)} \quad (1)$$

and the corresponding correlation length is $\xi \approx b[(1-2\chi)/n]^{2\nu-1} N_s^{2\nu}$.²⁹ The exponent ν is 0.5 for ideal chains, corresponding to θ -solvents, and ~ 0.6 for real chains, corresponding to good and athermal solvents.

The mapping of N_s as a function of $n^2\phi$, for different solvent qualities, is depicted in Figure 4a. The effect of various solvents

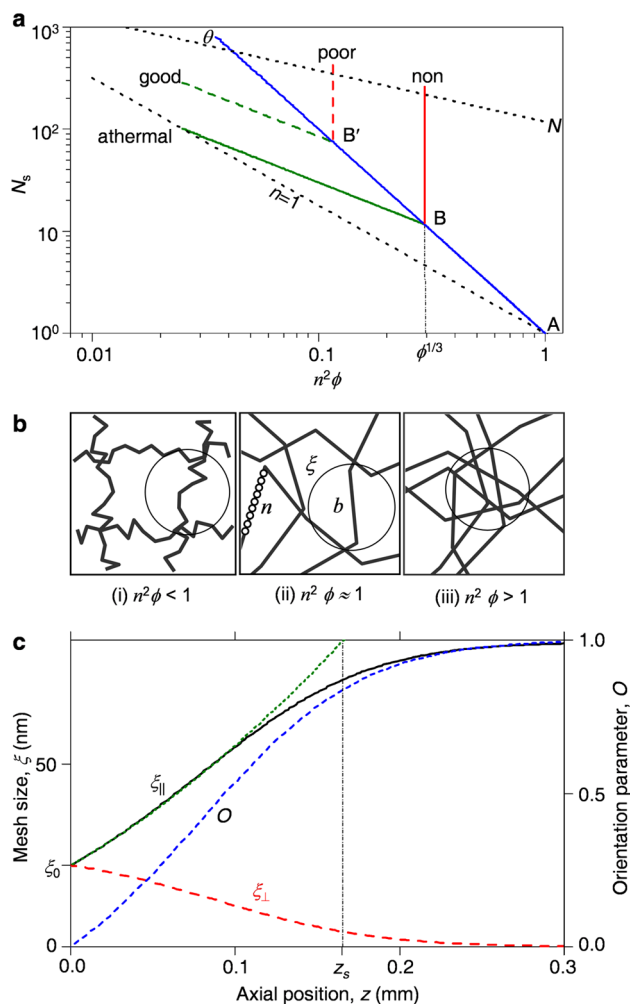


Figure 4. (a) Plot of N_s vs $n^2\phi$ and solvent quality. The θ -solvent curve marks the crossover between good and poor solvents. The dotted lines constitute the upper and lower limits for $\phi = 0.025$. Polymer molecular weight = 380,000 g/mol, equivalent to $N_{beads} = 730$. Points B and B', plotted for $\phi = 0.025$ for Flory's interaction parameter $\chi \cong 0$ and $\chi \cong 0.38$, respectively, mark the transition from ideal subchains (right) to real subchains (left). Prefactors are omitted for sake of simplicity. (b) Crossover (point A in part a) of the polymer network conformation with respect to the scale of the correlation length, ξ (circles) and the segment length, b : (i) regular semidilute, $\xi > b$, (ii) crossover, $\xi \approx b$, and (iii) different chains intermix within a single correlation volume, $\xi \approx b$. (c) Simulation of subchains during electrospinning. The axial mesh size $\xi_{||}$, radial mesh size ξ_{\perp} , and orientation parameter O are plotted vs the axial position, z , along the jet. $\xi_{||}$ is compared to the theoretical model (dotted line). The position close to full subchain extension is designated by z_s . Parameters used: ideal chain, $\phi = 0.025$, $n = 5$ beads, $d = 1.2$ nm, $\xi_0 \cong 20$ nm, $N_s = 14$ segments. Jet dynamics is from Figure S4 (see Supporting Information).

is discussed in detail in the Supporting Information. When the calculated N_s is above the N limit (upper dotted line, designating the overlap concentration ϕ^*), the polymer network is not sufficiently entangled for elastic stretching. The limit $n = 1$ (lower dotted line) designates the minimal selectable n value. For our solvent mixture (THF:DMSO 4:1 weight:weight), the interaction parameter can be estimated as $\chi \cong 0.38$,³⁰ and for our polymer volume fraction, $\phi = 0.025$, the transition from ideal to real chain conformation occurs at $n \cong 2.7$ beads (point B' in Figure 4a). The corresponding defects concentration (19% of monomers) is much higher than typical values ($< 10\%$, equivalent to $n > 5$),²⁷ and therefore the conformation of subchains is close to ideal (θ -solvent line in Figure 4a, right to point B'). At the high temperature limit (athermal solvent), the transition from ideal to real conformation occurs at $n \cong \phi^{-1/3} \cong 3.4$ beads (point B in Figure 4a), equivalent to 15% defects. Thus, as a chain is stiffer (higher n) it is more likely to be practically ideal, regardless of the solvent quality, provided that sufficient entanglement exists. At low concentration, when $n < \phi^{-1/2}$ (left to point A in Figure 4a), the subchain consists of many segments and does not interact with other chains [Figure 4b(i)]. When $n \approx \phi^{-1/2}$ (point A in Figure 4a), the correlation length ξ is of the same scale as the segment length b [Figure 4b(ii)].

However, when chains are not fully flexible, the correlation volume is not completely occupied by a single segment, and further increase of n and/or ϕ is possible. The network then crosses over to a state where different chains intermix within a single correlation volume [Figure 4b(iii)], increasing the probability of interchain overlap. The increased interaction between neighboring rigid segments may lead to nematic ordering and enhanced orientation, according to Onsager theory. For the volume fraction used in the experiment, $\phi = 0.025$, this crossover occurs at $n \cong 8.6$ beads, corresponding to defects concentration of $\sim 6\%$ of monomers.

On these bases, the evolution of the polymer conformation under dynamic tension can be described by a beads-and-spring lattice model and a 3D random walk simulation.²⁴ To this aim, the calculated number of segments per subchain, N_s , the initial correlation length, ξ_0 , and the pertaining experimental conditions are used as input to the simulations. The jet velocity is derived from the measured jet radius a , subjecting each subchain to a hydrodynamic force induced by the solvent, as well as to entropic elastic forces applied by its neighboring subchains.

The simulation results are presented in Figure 4c. It is seen that subchains fully extend within less than 1 mm from the jet start (position z_s), while contracting laterally, and their segments become fully oriented along the jet axis. The theoretical expression for the axial stretching (dotted line in Figure 4c), derived for linear elasticity, is given by²⁴ $\xi_{||} \approx (\nu/\nu_0)\xi_0 = (a_0/a)^2\xi_0$, (a_0 and ν_0 are the jet initial radius and velocity, respectively), whereas the orientational parameter (dashed line in Figure 4c) is defined as $O = (3/2)\langle \cos^2\delta \rangle - (1/2)$, δ being the angle between a rigid segment of the polymer molecule and the longitudinal axis. An example of the conformational evolution of a single subchain under the same conditions is shown in Figure 5.

The polymer chain is entangled with other chains in the solution (Figure 5a,b). Each subchain (an entanglement strand) starts from an equilibrium conformation at the jet start (Figure 5c), proceeds through intermediate stretching, and approaches full extension and lateral contraction (Figure 5d). The subchain

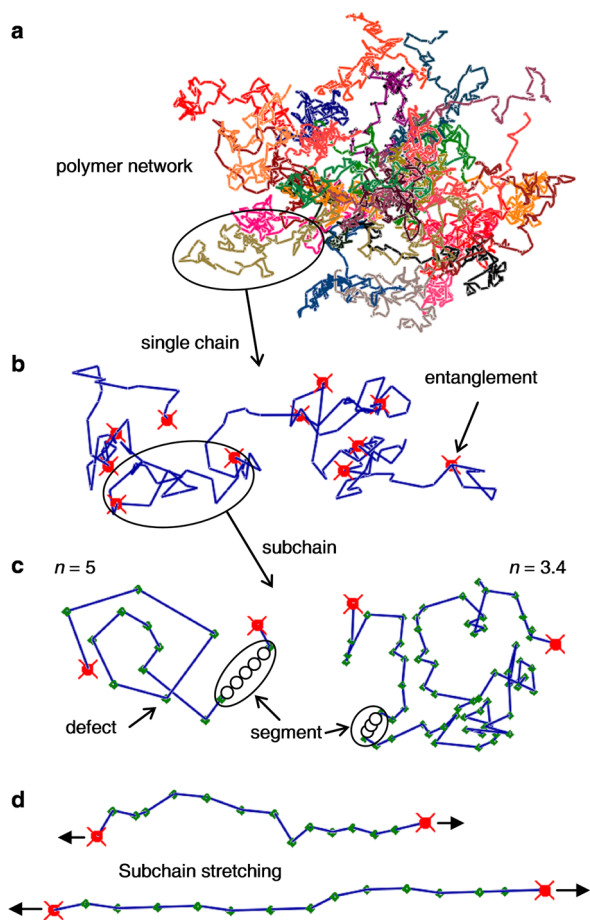


Figure 5. (a) Polymer network at rest. (b) Single chain with $N = 146$. (c) Examples of single subchains, left $N_s = 14$ ($n = 5$, 10% defects), right $N_s = 67$ ($n = 3.4$, 15% defects). (d) Stretched subchains, $N_s = 14$, $z = 0.08$ mm (top) and $z = z_s = 0.16$ mm (bottom).

conformation is sensitive to the average concentration of defects. A change in the defects concentration from 10% of monomers to 15% raises the subchain size from 14 to 67 segments and increases the correlation length. The lateral contraction of individual subchains affects the conformation of the whole polymer network, narrowing its radius a_p faster than the narrowing of the jet radius a . The dominant effect is of axial stretching and lateral contraction, resulting in compacting of the network toward the jet core. Thus, the model and simulation predict axial alignment at the jet center, while closer to the jet boundary the stretching effect is not dominant and other mechanisms prevail. These may include the influence of surface charges as recently investigated in polyamide 6 nanofibers.³¹ These charges can be tailored by changing the polarity of the applied voltage,³² and can lead to distinct properties such as enhanced surface energy compared to solution-processed films.

In our model, full extension is approached when $\xi_{II} \approx bN_s$, i.e. at the axial position z_s and a corresponding jet radius a_s . The axial position of full stretching, omitting the effect of n , scales as (Supporting Information):

$$\frac{z_s}{a_0} \sim N_s^{3/2} \begin{cases} \phi^{(\nu+2)/[2(3\nu-1)]} & \text{athermal solvent} \\ \phi^{11/6} & \theta\text{-solvent} \end{cases} \quad (2)$$

The estimated z_s for various solvent qualities, allowing the axial position of full stretching and consequently the resulting fiber properties for each particular nanofabrication experiment to be predicted, is shown in Figure 6a. Typically $z_s < 1$ mm and $a_0/a_s = 2-10$, close to the jet start. Considering that the final radius reduction ratios in electrospinning are typically 10^2-10^4 , substantial stretching occurs quite early in the process. For given polymer concentration and molecular weight, when n is larger (i.e., longer segments, equivalent to lower defects concentration), full stretching is approached at a higher jet radius and lower z_s ; however, at the same time, the number of entanglements per chain N/N_s is higher and therefore the solution viscosity will be larger, increasing z_s . In contrast to the radius reduction ratio a_0/a_s , the axial position z_s is strongly affected by the jet rheology, resulting in a concentration dependence with a large positive exponent, as well as added dependence on the molecular weight (Figure 6a). In addition to its dependence on the molecular weight and concentration as expressed in eq 2, z_s strongly depends on the intensity of the electrostatic field E and the jet initial velocity v_0 . It can be shown that this dependence may be approximated by $z_s \sim v_0^{1/2} E^{-1}$, meaning that a high strain rate, caused by high E and low v_0 , should result in earlier stretching.

A substantial axial stretching of chains is therefore predicted during the initial stage of the elongational flow, causing lateral contraction of the polymer network toward the center of the jet, as well as orientation of chain segments along the jet axis. Similar results obtained for fully flexible chains (particular case with $n = 1$) have been confirmed by X-ray imaging of high strain rate electrified jets.^{24,25} In electrospinning, the electric field provides the flow of the semidilute solution with a characteristic increasing velocity along the jet axis, with a strain rate that continuously increases the elastic stretching of the polymer network and reduces network relaxation. Our model shows that full chain stretching is approached at a higher jet radius as the chain is stiffer, at a region where the mass loss rate due to evaporation is still low.

When stretching is less dominant (e.g., at low electric field and high flow rate), the rapid solvent evaporation can adversely affect the polymer matrix, creating a porous nanofiber structure. Dominant evaporation can also lead to a rapid solidification of the jet surface, limiting further solvent loss from the core.³³⁻³⁵ The presence of residual solvent content in the jet core would allow for chain relaxation, thus disfavoring the retention of alignment in the core as recently reported for electrospun polyvinyl-alcohol fibers.³⁶ Instead, when stretching is dominant as in the present case, the polymer network compacts toward the center, producing an increase of the density close to the jet axis.²⁶ The here observed ribbons (Figure 1) are hence likely affected by concurring effects rather than jet skin collapse, such as flattening and relaxation processes occurring at the impact onto the substrate. This would be consistent with the presence of a slowly evaporating solvent component, i.e. with a jet time-of-flight which is comparable with the drying time scale,^{35,37} and supported by the joints observed in SEM micrographs of intersecting deposited fibers (e.g., Figure 1b,c).

This description is in agreement with polarization modulation measurements (Figure 3), showing a change in the sign of the dichroic ratio along the fiber radius, and indicating a preferred axial alignment of molecules at the fiber core, whereas molecules closer to the fiber boundary possess a preferred radial alignment. Thus, at the jet center axial stretching is dominant, and one can anticipate a propensity for interchain interaction

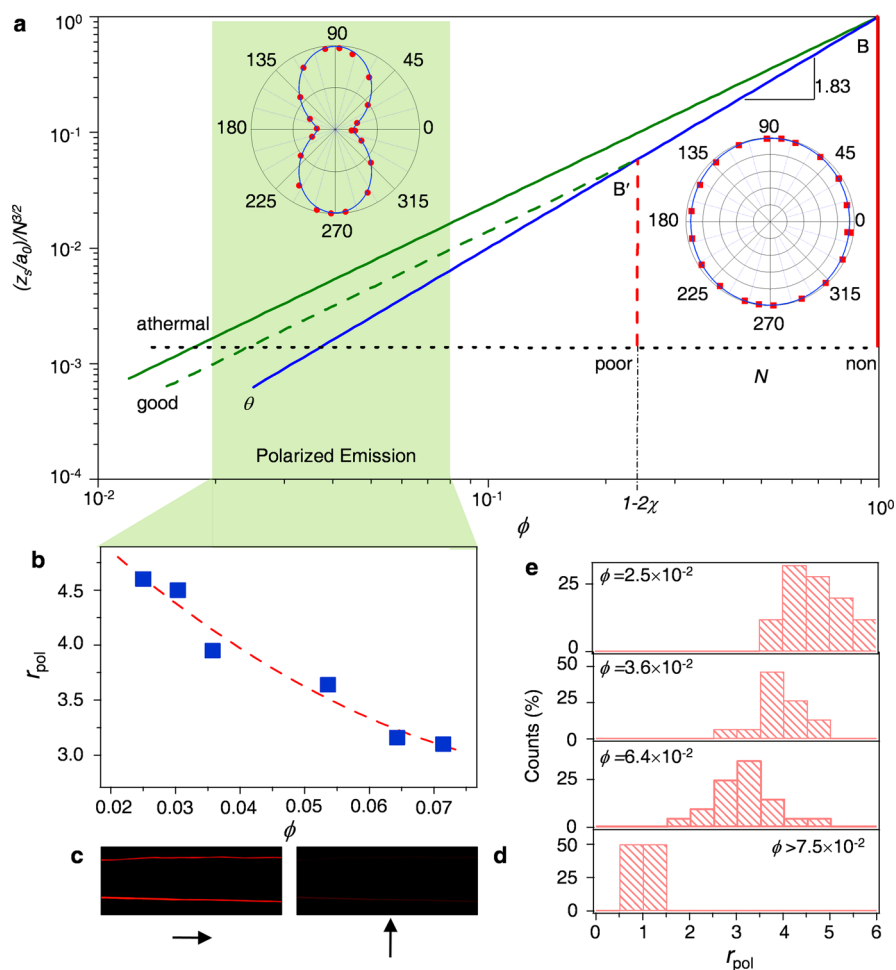


Figure 6. (a) Plot showing the axial position where subchains approach full extension, z_s/a_0 , normalized by $N^{3/2}$, vs the polymer volume fraction ϕ and solvent quality, for $n = 1$. The dotted line constitutes the lower limit imposed by $N_s < N$. Prefactors are omitted for sake of simplicity. Points B and B' are explained in Figure 4a. Insets: Plot of the normalized nanofiber emission intensity vs the angle between the fiber and the analyzer axis, measured on fibers electrospun from a solution with $\phi = 0.03$ (left inset) and on a sprayed film for comparison (right inset). (b) Polarization ratio, r_{pol} vs solution volume fraction, ϕ . The dashed line is a guide for the eyes. An unpolarized sample (sprayed film) has $r_{pol} = 1$. (c, d) Confocal images of nanofiber polarized emission. The laser-excited emission is filtered through an analyzer with axis (highlighted by arrows) parallel and perpendicular to the fiber axis, respectively. (e) Experimental distributions of the nanofiber polarization ratio, r_{pol} , at different polymer concentrations.

and π - π stacking and consequently high extent of local crystallinity.³⁸ At the boundary region of the jet, where the polymer concentration is reduced,^{25,26} entanglement may be low or nonexistent, allowing partial or full relaxation of chains back to their coil-shaped equilibrium state. This mechanism is also supported by a recent study on entanglement loss in extensional flow,³⁹ showing that the electrospinning process causes partial untangling of the polymer network when stretching is faster than the chains relaxation time.

Overall, full extension of the network occurs at an earlier stage of the jet (lower z_s) if the solution initial concentration, the polymer molecular weight, and the solvent quality are lower, accounting for lower network entanglement. Under such conditions, the likelihood that the extended conformation, and the associated axial molecular alignment, will partially remain in the polymer structure after solidification is higher. This enables tailoring the physical properties of fibers, such as the far-field, macroscale emission from fibers. The $z_s(\phi)$ diagram of Figure 6a clearly relates the chain alignment, and hence the resulting polarization, to the polymer volume fraction (i.e., solution concentration). Indeed, by our approach we obtain a fine-

tuning of the polarization ratio of the fiber emission ($r_{pol} = I_{||}/I_{\perp}$, given by the ratio between the photoluminescence intensity parallel, $I_{||}$, and perpendicular, I_{\perp} , to the fiber axis, respectively), increasing up to about 5 by gradually decreasing the solution concentration down to a volume fraction $\phi = 0.025$, as shown in Figure 6b–e. This demonstrates the possibility of tailoring specific fiber properties by the relevant process parameters. The ultimate r_{pol} values may also benefit from the higher density in the core,²⁶ as well as from electronic energy-transfer mechanisms, which strongly affect the emission properties of conjugated polymers.^{40,41} Conjugated polymer fibers frequently show red-shifted absorption compared to spincoated films (Figure S1a and ref 42), a property consistent with a longer effective conjugation length consequence of the stretched conformation. In fact, the elongational dynamics of solutions leads to extended structures having interchain alignment. The bonding defects concentration, $(2n)^{-1}$ of monomers, determines chain flexibility, and appears as a possible key factor in controlling the desired morphology.

CONCLUSIONS

In summary, anisotropy at nanoscale is investigated in polymer fibers by polarization modulation SNOM absorption measurements, evidencing a variation of molecular orientation from axial to radial upon moving from the fiber axis to its surface. Modeling the evolution of the conformation of the chains network allows us to identify key parameters for controlling molecular alignment, as demonstrated by the fine control of the emission polarization. The found complex internal structure and assessment of the key influencing process variables open new perspectives for tailoring the molecular morphology and resulting fiber properties.

ASSOCIATED CONTENT

Supporting Information

Theoretical model rational and details, fibers optical properties, and technical details about SNOM measurements. This material is available free of charge via the Internet at <http://pubs.acs.org>.

AUTHOR INFORMATION

Corresponding Authors

*E-mail: (A.C.) andrea.camposeo@nano.cnr.it.

*E-mail: (I.G.) green_is@netvision.net.il.

*E-mail: (D.P.) dario.pisignano@unisalento.it.

Author Contributions

[#]These authors contributed equally.

Notes

The authors declare no competing financial interest.

ACKNOWLEDGMENTS

We gratefully acknowledge the financial support of the United States-Israel Binational Science Foundation (BSF Grant 2006061), the RBNI-Russell Berrie Nanotechnology Institute, and the Israel Science Foundation (ISF Grant 770/11). The research leading to these results has received funding from the European Research Council under the European Union's Seventh Framework Programme (FP/2007-2013)/ERC Grant Agreement No. 306357 (ERC Starting Grant "NANO-JETS"). The authors also gratefully thank S. Pagliara for sample preparation, E. Caldi for assistance in the SNOM measurements, S. Girardo for imaging of the polymer jet, and V. Fasano for confocal images.

REFERENCES

- (1) Dvir, T.; Timko, B. P.; Kohane, D. S.; Langer, R. *Nat. Nanotechnol.* **2011**, *6*, 13–22.
- (2) Shannon, M. A.; Bohn, P. W.; Elimelech, M.; Georgiadis, J. G.; Mariñas, B. J.; Mayes, A. M. *Nature* **2008**, *452*, 301–310.
- (3) Lu, W.; Zu, M.; Byun, J.-H.; Kim, B.-S.; Chou, T.-W. *Adv. Mater.* **2012**, *24*, 1805–1833.
- (4) Veedu, V. P.; Cao, A.; Li, X.; Ma, K.; Soldano, C.; Kar, S.; Ajayan, P. M.; Ghasemi-Nejhad, M. N. *Nat. Mater.* **2006**, *5*, 457–462.
- (5) Shen, S.; Henry, A.; Tong, J.; Zheng, R.; Chen, G. *Nat. Nanotechnol.* **2010**, *5*, 251–255.
- (6) Reneker, D. H.; Chun, I. *Nanotechnology* **1996**, *7*, 216–223.
- (7) Arinstein, A.; Burman, M.; Gendelman, O.; Zussman, E. *Nat. Nanotechnol.* **2007**, *2*, 59–62.
- (8) Collins, R. T.; Jones, J. J.; Harris, M. T.; Barasan, O. A. *Nat. Phys.* **2008**, *4*, 149–154.
- (9) Bhat, P. P.; Appathurai, S.; Harris, M. T.; Pasquali, M.; McKinley, G. H.; Barasan, O. A. *Nat. Phys.* **2010**, *6*, 625–631.
- (10) Yarin, A. L.; Koombhongse, S.; Reneker, D. H. *J. Appl. Phys.* **2001**, *90*, 4836–4846.
- (11) Facchetti, A. *Nat. Mater.* **2013**, *12*, 598–600.
- (12) Richard-Lacroix, M.; Pellerin, C. *Macromolecules* **2013**, *46*, 9473.
- (13) Prins, P. P.; Grozema, F. C.; Schins, J. M.; Patil, S.; Scherf, U.; Siebbeles, L. D. A. *Phys. Rev. Lett.* **2006**, *96*, 146601.
- (14) Kim, F. S.; Ren, G.; Jenekhe, S. A. *Chem. Mater.* **2011**, *23*, 682–732.
- (15) Wang, S.; Kappl, M.; Liebewirth, I.; Müller, M.; Kirchhoff, K.; Pisula, W.; Müllen, K. *Adv. Mater.* **2012**, *24*, 417–420.
- (16) Martini, I. B.; Craig, I. M.; Molenkamp, W. C.; Miyata, H.; Tolbert, S. H.; Schwartz, B. J. *Nat. Nanotechnol.* **2007**, *2*, 647–652.
- (17) Dubin, F. F.; Melet, R.; Barisien, T.; Grousson, R.; Legrand, L.; Schott, M.; Voliotis, V. *Nat. Phys.* **2006**, *2*, 32–35.
- (18) Dersch, R.; Liu, T.; Schaper, A. K.; Greiner, A.; Wendorff, J. H. *J. Polym. Sci., Polym. Chem.* **2003**, *41*, 545–553.
- (19) Bellan, L. M.; Craighead, H. G. *Polymer* **2008**, *49*, 3125–3129.
- (20) Pagliara, S.; Vitiello, M. S.; Camposeo, A.; Polini, A.; Cingolani, R.; Scamarcio, G.; Pisignano, D. *J. Phys. Chem. C* **2011**, *115*, 20399–20405.
- (21) Eisele, D. M.; Knoester, J.; Kirstein, S.; Rabe, J. P.; Vanden Bout, D. A. *Nat. Nanotechnol.* **2009**, *4*, 658–663.
- (22) O'Carroll, D.; Iacopino, D.; Redmond, G. *Adv. Mater.* **2009**, *21*, 1160–1165.
- (23) Pomraenke, R.; Ropers, C.; Renard, J.; Lienau, C.; Lüer, L.; Polli, D.; Cerullo, G. *Nano Lett.* **2007**, *7*, 998–1002.
- (24) Greenfeld, I.; Arinstein, A.; Fezzaa, K.; Rafailovich, M. H.; Zussman, E. *Phys. Rev. E* **2011**, *84*, 041806.
- (25) Greenfeld, I.; Fezzaa, K.; Rafailovich, M. H.; Zussman, E. *Macromolecules* **2012**, *45*, 3616–3626.
- (26) Camposeo, A.; Greenfeld, I.; Tantussi, F.; Moffa, M.; Fuso, F.; Allegrini, M.; Zussman, E.; Pisignano, D. *Nano Lett.* **2013**, *13*, 5056–5052.
- (27) Hu, D.; Yu, J.; Wong, K.; Bagchi, B.; Rossky, P. J.; Barbara, P. F. *Nature* **2000**, *405*, 1030–1033.
- (28) The exponent is 0.5 for ideal chains, corresponding to Θ -solvents, and ~ 0.6 for real chains, corresponding to good and athermal solvents.
- (29) The prefactors, of the order of unity, are omitted for clarity.
- (30) Mark, J. E. *Physical properties of polymers handbook*; AIP Press: Woodbury, NY, 1996. Since THF is a good solvent for MEH-PPV while DMSO is a poor solvent, the interaction parameter may be slightly higher than 0.38.
- (31) Stachewicz, U.; Barber, A. H. *Langmuir* **2011**, *27*, 3024.
- (32) Stachewicz, U.; Stone, C. A.; Willis, C. R.; Barber, A. H. *J. Mater. Chem.* **2012**, *22*, 22935.
- (33) Koombhongse, S.; Liu, W.; Reneker, D. H. *J. Polym. Sci., Part B: Polym. Phys.* **2001**, *39*, 2598–2606.
- (34) Arinstein, A.; Zussman, E. *Phys. Rev. E* **2007**, *76*, 056303.
- (35) Pai, C.-L.; Boyce, M. C.; Rutledge, G. C. *Macromolecules* **2009**, *42*, 2102.
- (36) Stachewicz, U.; Bailey, R. J.; Wang, W.; Barber, A. H. *Polymer* **2012**, *53*, 5132.
- (37) Wu, X.-F.; Salkovskiy, Y.; Dzenis, Y. A. *Appl. Phys. Lett.* **2011**, *98*, 223108.
- (38) Craig, I. M.; Tassone, C. J.; Tolbert, S. H.; Schwartz, B. J. *J. Chem. Phys.* **2010**, *133*, 044901.
- (39) Greenfeld, I.; Zussman, E. *J. Polym. Sci., Part B: Polym. Phys.* **2013**, *51*, 1377.
- (40) Hwang, I.; Scholes, G. D. *Chem. Mater.* **2011**, *23*, 610.
- (41) Nguyen, T.-Q.; Wu, J.; Doan, V.; Schwartz, B. J.; Tolbert, S. H. *Science* **2000**, *288*, 652.
- (42) Li, D.; Babel, A.; Jenekhe, S. A.; Xia, Y. *Adv. Mater.* **2004**, *16*, 2062–2066.